Information Entropy Guided Height-aware Histogram for Quantization-friendly Pillar Feature Encoder

Sifan Zhou[1†], *Student Member, IEEE,* Zhihang Yuan[2†], Dawei Yang[2], Ziyu Zhao[1], Xing Hu[2], Yuguang Shi[1], Xiaobo Lu[1*], Qiang Wu[2] *Senior Member, IEEE,*

***Abstract*—Real-time and high-performance 3D object detection plays a critical role in autonomous driving and robotics. Recent pillar-based 3D object detectors have gained significant attention due to their compact representation and low computational overhead, making them suitable for onboard deployment and quantization. However, existing pillar-based detectors still suffer from information loss along height dimension and large numerical distribution difference during pillar feature encoding (PFE), which severely limits their performance and quantization potential. To address above issue, we first unveil the importance of different input information during PFE and identify the height dimension as a key factor in enhancing 3D detection performance. Motivated by this observation, we propose a height-aware pillar feature encoder, called PillarHist. Specifically, PillarHist statistics the discrete distribution of points at different heights within one pillar with the information entropy guidance. This simple yet effective design greatly preserves the information along the height dimension while significantly reducing the computation overhead of the PFE. Meanwhile, PillarHist also constrains the arithmetic distribution of PFE input to a stable range, making it quantization-friendly. Notably, PillarHist operates exclusively within the PFE stage to enhance performance, enabling seamless integration into existing pillar-based methods without introducing complex operations. Extensive experiments show the effectiveness of PillarHist in terms of both efficiency and performance.**

I. Introduction

LiDAR-based 3D object detection plays a pivotal role in various applications [1]–[5], particularly in autonomous driving and robotics. It is important to detect the objects in the surrounding environment fastly and accurately, which places a high demand for both performance and latency. Existing mainstream methods can be categorized into two types based on the point cloud representation: **(1)** point-based [6]–[10] and **(2)** grid-based models [11], [12], [12]–[16]. Point-based models generally inherit the success in point cloud representation learning using deep neural networks [17], [18] and detect objects directly from raw points. However, these methods often face challenges in real-time onboard deployment as they often require point query/retrieval in 3D space (*e.g.*, PointNet++ [19]). Grid-based methods rasterize the points into regular grid (voxel/pillar) and employ 2D or 3D convolution for feature learning. Compared to voxel-based methods, pillar-based detectors exhibit a more compact grid representation and can seamlessly integrate advanced 2D detection techniques without much modification. Therefore, those methods offer a favorable trade-off between performance and speed, making them highly suitable for practical deployment in autonomous systems. Furthermore, it is equally crucial to deploy them on resource-limited edge devices by improve their efficiency (*e.g.*, reduce memory and computation cost).

The Pillar Feature Encoding (PFE) module plays a huge role in pillar-based networks [13], [20]–[23]. Its main purpose is to transform the input point clouds, which are initially unordered (x, y, z, intensity) information, into pillars with a regular spatial arrangement. Each pillar has a fixed length of feature dimensions. In this paper, we observe that existing pillar-based methods suffer from two key problem in PFE module. ❶ Information loss significantly hampers their performance. ❷ Encoding scheme leads to a large variation of activations, making quantization challenging. As shown in Figure 1, the problem ❶ can be attributed to two factors: (1) **Lack of detailed height-aware feature encoding**. The height information is not well handled, resulting in an incomplete representation of the 3D scene. It is difficult to distinguish the height differences in various situations, like a pedestrian and a person standing on a car. (2) **Max-pooling operator causes the loss of height information**. The adoption of max-pooling operations within each pillar to derive pillar features leads to a loss of detailed information, which limits the ability of the encoded features to distinguish different objects.

The problem ❷ can be attributed the various arithmetic range of the PFE input. For instance, in nuScenes [24] dataset, the input of PFE includes $\hat{p_i} = \{[x_i, y_i, z_i, r_i, x_i^m, y_i^m, z_i^m, x_i^c, y_i^c, z_i^c] \in \mathbb{R}^{N_v \times 10}\}$, where $[x_i, y_i, z_i] \in [-51.2, 51.2]$ is the point coordinates, $r_i \in [0, 255]$ is the intensity, $[x_i^m, y_i^m, z_i^m] \in [-0.2, 0.2]$ (pillar size = 0.2m) denotes the offset of $[x_i, y_i, z_i]$ and the mean value of $[x_i, y_i, z_i]$ within one pillar, and $[x_i^c, y_i^c, z_i^c] \in [-4.0, 4.0]$ is the spatial offset of $[x_i, y_i, z_i]$ and the pillar center. Details refer to Sec III-A. The different part of input represents the global- and local-contextual information, but exhibit significant difference in numerical distribution. Therefore, the arithmetic disparity makes it more susceptible to the effects of quantization (*e.g.*, clipping error).

To address the above issues, we propose a novel quantization-aware pillar feature encoder called PillarHist. It leverages a histogram technique to encode the height-aware information of each pillar into multiple bins, and the number of points

This work was supported by the National Natural Science Foundation of China (No.62271143), and the Big Data Computing Center of Southeast University.

Sifan Zhou, Ziyu Zhao, Yuguang Shi and Xiaobo Lu are with School of Automation, Southeast University and the Key Laboratory of Measurement and Control of Complex Systems of Engineering, Ministry of Education, Nanjing 210096, China. Zhihang Yuan, Dawei Yang, Xing Hu and Qiang Wu are from Houmo AI, Nanjing 210046, China. (E-mail: {sifanjay, hahnyuan, zhaoziyu.950207}@gmail.com, {dawei.yang, xing.hu, qiang.wu}@houmo.ai, syg@seu.edu.cn, xblu2013@126.com) (†Equal contribution. *Corresponding author.)

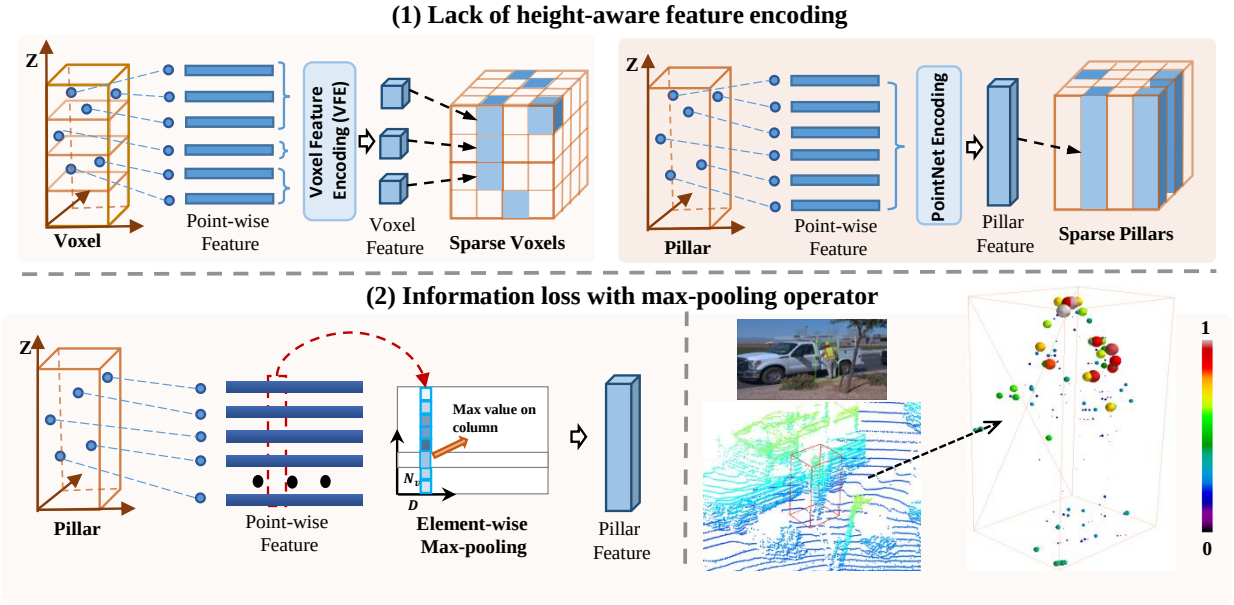

Fig. 1. The drawbacks of pillar feature encoding are as follows: (1) Compared with the voxel feature encoding, the encoding process of pillars lacks height awareness, as it does not explicitly model the height dimension of the input point cloud. (2) PFE employs element-wise max-pooling operation, which inevitably results in information loss. As illustrated in the right side of (2), the max-pooling operation tends to preserve the feature information of points with higher height values within a pillar while disregarding points with lower height values, resulting in the loss of geometric information within the pillar.

falling within each bin is counted. The resulting histogram representation provides both semantic and geometric information from the height dimension. PillarHist incorporates the LiDAR reflection intensity of each point to obtain a weighted histogram of intensity, which adds distinguished height-aware information for object detection. These histograms, along with the pillar center coordinates, are concatenated and passed through a linear layer to obtain a feature vector representing the pillar. Specially, PillarHist constrains the arithmetic distribution of PFE input to a stable range, making it friendly for further quantization. Besides, by operating linear projection at the pillar level instead of individual points, PillarHist significantly reduces the computation overhead, resulting in improved efficiency. It can be seamlessly integrated into existing pillar-based methods as a plugin module. Extensive experiments demonstrate the effectiveness of our proposed PillarHist in terms of both efficiency and performance. The contributions of our method can be summarised as follows:

- We conduct a thorough analysis of existing Pillar Feature Encoding (PFE) modules. Our findings indicate that they suffer from a loss of information in the height dimension and exits large variation of activation for model quantization.
- We propose a novel PFE module called PillarHist, which can mitigate the height information loss and reduce the computation cost of PFE. It is noteworthy that we make it a plugin module to conveniently insert into existing mainstream pillar-based methods while seamlessly boosting their performance.
- We explore the quantization-friendly properties of PillarHist. PillarHist could effectively eliminate the severe performance degradation after quantization caused by the raw PFE, bringing quantization performance gain effortlessly.
- We conduct extensive experiments to evaluate the effectiveness of PillarHist. Our results showed that it achieved an average improvement of approximately 1.5 in AP across various baselines in KITTI and 0.7 NDS in nuScenese dataset without extra latency.

In the following sections, we provide a detailed overview of related works in 3D object detection, and comprehensively describe our proposed PillarHist method. Subsequently, we present the experimental setup, evaluation results, and a thorough analysis of the obtained results. Finally, we conclude our paper and provide insights into potential future research directions of 3D object detection.

II. Related Work

A. Grid Feature Encoding.

Grid feature encoding is an essential module for grid-based 3D object detectors, and directly affects model's accuracy [25], [26]. Several approaches have been proposed to extract features from two types of grid representations: Voxel and Pillar. VoxelNet [11] is a pioneering work that proposes a novel voxel feature encoding (VFE) layer to extract features. Many studies, including [10], [27]–[33], also adopt similar voxel encoding strategy. Similiar to voxel, pillars can be viewed as special voxels that do not have the vertical division. PointPillars [13] is a seminal work that leverages PointNet [17] for extracting point features within pillars and employs a maxpooling operator to obtain pillar features. Due to its compact representation, subsequent works [20]–[23], [34]–[37] have widely adopted the pillar representation following PointPillars [13]. TANet [36] proposes a Triple Attention (TA) module, which separately adopts Point-wise/Channel-wise/Voxel-wise attention operations to focus on the spatial correlations among the points inside each voxel. Although effective, the TA module operates on point-wise level and

inevitably using max-pooling operation, which bring a large computational burden and also limit the pillar representations. PiFeNet [37] proposes the Pillar Aware Attention (PAA) module, which has a more lightweight design compared to the TA module in TANet. The PAA module uses channel-wise and point-wise attention to learn expressive features, and design a task-aware attention to reorganise the pillar feature. However, PiFeNet still adopts pooling (max- and avg-pool) operations, and its attention operations are still on point-wise level, which also hinders its inference speed and lightweight application. Recently, PillarNet [21] designs a dynamic PFE module with less information loss and show the powerful "backbone-neck-head" architecture design. FastPillars [23] introduces a MAPE module with attentive-pooling to preserve more fine-grained geometrics. However, the PFE module in these methods do not explicitly consider the detailed height-aware information, and they all employ element-wise max-pooling or similar pooling operations, which still leading to information loss. In this paper, we focus on enhancing detailed height-aware information and mitigate the information loss caused by pooling operations.

B. Quantization for 3D Object Detection.

With the wide application of 3D object detection in autonomous driving and robotics, some quantization methods are designed to improve inference speed for onboard deployment applications. With the advance of quantization techniques based on RGB image, QD-BEV [38] achieves smaller size and faster speed than baseline BevFormer [39] using Quantization-Aware Training (QAT) and distillation on multi-camera 3D detection tasks. For LiDAR-based 3D detection, [40] find that directly using INT8 quantization for 2D CNN will bring significant performance drop on PointPillars [13], where the reduction is even more severe for the entropy calibrator. Besides, BiPointNet [41] is a binarization quantization method, which focuses on classification and segmentation tasks based on point cloud captured from small CAD simulation. Recently, LiDAR-PTQ [2] unveils the root cause of performance collapse in the quantization of LiDAR-based detection and propose an effective PTQ method. However, some advanced quantization techniques [42]–[45] are still required to find optimal quantization parameter in LiDAR-PTQ. Different with LiDAR-PTQ, which is a PTQ method tailored for point cloud detection, our PillarHist aim to make the distribution of weights as well as the processed data of an arbitrary distribution shall be quantization friendly.

III. Our Approach

A. Preliminary

LiDAR-based 3D Object Detection. We present the basic task definitions of LiDAR-based 3D object detection before introducing the detailed method. Given a point set with N points in the 3D space, which is defined as $\mathbf{P} = \{\mathbf{p}_i = [x_i, y_i, z_i, r_i]^T \in \mathbb{R}^{N\times 4}\}$, where x_i, y_i, z_i denote the coordinate values of each point along the axes X, Y, Z, respectively, and r_i is the LiDAR reflection intensity. Given a set of objects in the 3D scene $\mathbf{B} = \{\mathbf{b}_j = [x_j, y_j, z_j, h_j, w_j, l_j, r_j, c_j]^T \in \mathbb{R}^{M\times 8}\}$, where M is the total number of objects, b_i is the i-th object in the scene, x_j, y_j, z_j is the object's center, h_j, w_j, l_j is the object's size, r_j is the object's heading angle and c_j is the object's class. The task of 3D object detection is to predict the 3D bounding boxes $\mathbf{B}$ from the point cloud $\mathbf{P}$ in driving scenarios accurately.

Point Cloud Pillarization. Our aim is to transform the point cloud $\mathbf{P}$ into a regular 3D pillar representation. Assuming that $\mathbf{P}$ is in the 3D space with the range of L, W, H along the x, y, z axes, respectively, The point cloud $\mathbf{P}$ is uniformly partitioned into a specific pillar grid of size (δ_x, δ_y,H), we can compute the no-empty pillar index using:

$$(x_{int}, y_{int}, z_{int}) = (\lfloor \frac{x_i}{\delta_x} \rceil, \lfloor \frac{y_i}{\delta_y} \rceil, \lfloor \frac{H}{2} \rceil), i = 0...N-1 \quad (1)$$

where $\lfloor \cdot \rceil$ is the floor operation, $x_{int}, y_{int}, z_{int}$ is the 3D pillar index of p_i after pillarization. Notably, point cloud $\mathbf{P}$ is only pillarized along the XY plane without the height dimension. Let $V = \{v_i = [x_i, y_i, z_i, r_i] \in \mathbb{R}^{N_v\times 4}\}, i \in \{1, ..., N_v\}$, be a non-empty pillar contains N_v points, N_v is number of points in pillar V.

Pillar Feature Encoding. Pillar Feature Encoding (PFE) plays a crucial role in pillar-based 3D detection methods [13], [21], [23], directly impacting the representation learning of BEV feature and final detection accuracy. Here, taking PointPillars [13] as an example, we illustrate the details of PFE. **Firstly**, the points in each pillar are initially concatenated along the channel dimension to form $\hat{p_i} = \{[x_i, y_i, z_i, r_i, x_i^m, y_i^m, z_i^m, x_i^c, y_i^c, z_i^c] \in \mathbb{R}^{N_v\times 10}\}$, where $[x_i, y_i, z_i]$ is the original point coordinates in the ego frame, $[x_i^m, y_i^m, z_i^m]$ denotes the offset of p_i from the mean of the xyz coordinates of all points within the current pillar, and $[x_i^c, y_i^c, z_i^c]$ is the offset of p_i from the current pillar center. Notably, for each pillar, a sampling or padding strategy is employed to ensure that all pillars contain the same number of points. **Secondly**, the concatenated point-wise features $\hat{p_i}$ within a non-empty pillar V are mapped to the high-dimensional feature space using MLP layers. This process can be mathematically formulated as:

$$p_i^c = m(\hat{p_i}; w_m) \quad (2)$$

where the function $m(\cdot)$ denotes MLP, w_m denotes the learnable weights of $m(\cdot)$, and $p_i^c \in \mathbb{R}^{N_v\times D}$ is the point-wise feature. **Thirdly**, an element-wise max-pooling operation is applied along the dimension of point features, which is formulated as:

$$f^m = max(p_i^c) \quad (3)$$

where $max(\cdot)$ means the max-pooling operator, and $f^m \in \mathbb{R}^D$ is the resulting feature vector to represent non-empty pillar V. **Finally**, a non-empty pillar $V \in \mathbb{R}^{N_v\times 4}$ consisting of N_v points is encoded into a feature vector $f^m \in \mathbb{R}^D$.

B. What Kind of Information Do We Need in PFE?

(1) Height Information is More Important. As aforementioned, the pioneering pillar-based method PointPillars [13] concatenates two extra relation information along the channel dimension of the raw point cloud, i.e. ($[x_i^m, y_i^m, z_i^m]$) and ($[x_i^c, y_i^c, z_i^c]$). Here, we decouple the input information along

TABLE I
ABLATION RESULTS OF DIFFERENT INPUT FOR PFE IN POINTPILLARS ON THE KITTI *val* SET IN AP_{3D} (R40) AND AP_{3D} (R11) FOR CAR.

(x_i, x_i^m, x_i^c)	(y_i, y_i^m, y_i^c)	(z_i, z_i^m, z_i^c)	$3D_{R40}$ mAP	Easy	Mod.	Hard	$3D_{R11}$ mAP	Easy	Mod.	Hard
✔			57.50	67.98	53.30	51.24	58.20	67.94	53.82	52.85
	✔		59.40	69.85	55.45	52.89	59.96	69.41	56.17	54.31
		✔	**79.63**	86.68	77.62	74.59	**79.15**	86.67	76.49	74.28
PointPillars			79.98	87.08	77.90	74.97	79.43	86.25	76.76	75.02

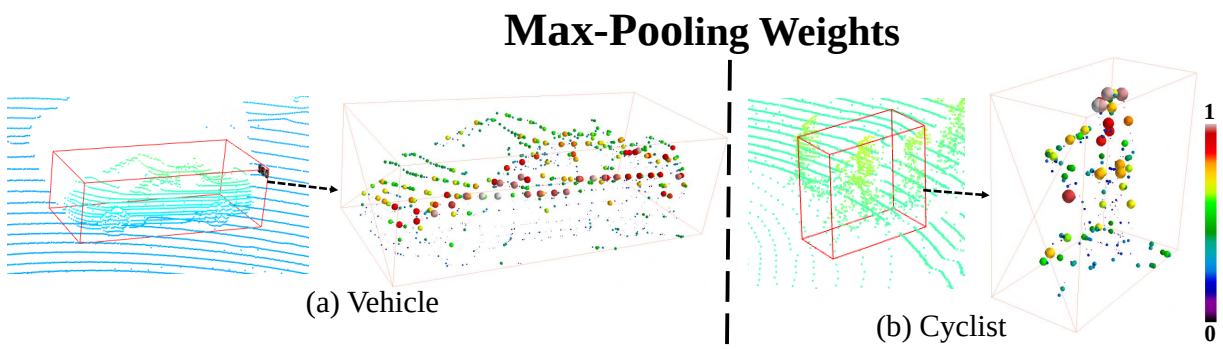

Fig. 2. Visualization of the weights on (a) vehicle and (b) cyclist using Max-pooling in PFE. The size of points means scores. The point will be paid more attention if it has a higher score. Compared with original object's points, max-pooling operator in PFE inevitably result in the loss of fine-grained information the object and local geometries. Best viewed in color.

the x, y, and z axes, respectively. aiming to explore their impact on the final 3D detection performance.

As shown in Table I, when we only input the information along the x axis (x_i, x_i^m, x_i^c) or the information along the y axis (y_i, y_i^m, y_i^c), there is a significant degradation in the final 3D detection performance, The former results in a large decrease of 22.48 mAP of $3D_{R40}$ and 21.23 mAP of $3D_{R11}$, while the latter leads to a large decrease of 20.58 mAP of $3D_{R40}$ and 19.47 mAP of $3D_{R11}$. However, when we only input the information along the z axis (z_i, z_i^m, z_i^c), it also achieves comparable performance with the baseline. This indicates that in the pillar feature encoding process, the information along the z axis, $a.k.a$ the height dimension, plays a key role in the final 3D detection performance.

(2) Pillar Information Loss by Max-pooling. As mentioned in the introduction (Section I), current pillar-based methods [13], [20], [21], [23] heavily rely on max pooling to aggregate point features within each pillar. However, this max-pooling operation (as shown in Equation 3) inevitably leads to the loss of detailed information, particularly the local geometric patterns that play an important role in object recognition. To illustrate this point, we have visualized the effect of the max-pooling operation in Figure 2. In the figure, we represent the points that are more likely to be selected by max pooling as larger and red spheres. It is evident from the visualization that a significant number of points are not selected after the max-pooling operation, while only a small fraction of points have a high probability of being chosen. This comparison clearly shows that the max-pooling operator results in a substantial loss of object geometry information compared to the original points of the object.

C. PillarHist: Information Entropy Guided Height-aware Discrete Histogram for PFE

Hence, the challenge lies in finding a pillar encoding method that addresses these problems. Our goal is to develop a pillar feature encoding approach that possesses the following two key characteristics:

❶ It should eliminate the requirement for sampling operations while still maintaining the ability to capture the height-awareness of the points within each pillar. This means that the encoding method should effectively handle the variation in point density across different height levels within a pillar.

❷ It should keep the semantic and geometric information within the pillar, without resorting to max pooling or similar pooling operations. This is important to ensure that the encoded representation retains the relevant details and characteristics of the original pillar.

To achieve these objectives, we propose leveraging the histogram distribution. We can effectively capture the distribution of points within a pillar at different height levels. This allows us to maintain the height-awareness of the points without the need for sampling operations. The implementation of the histogram operation is straightforward. Initially, we divide the height range of the pillar into multiple bins, where each bin corresponds to a specific range of heights. For instance, if the pillar's height spans from 0 to 10 meters, we can partition it into several bins such as 0-1m, 1-2m, 2-3m, and so forth. Next, we proceed to count the number of points that fall within each bin for a given pillar. This counting process yields a count value for each bin, indicating the number of points residing within that particular height range. For instance, if a larger number of points are found in the lower height range bins, it

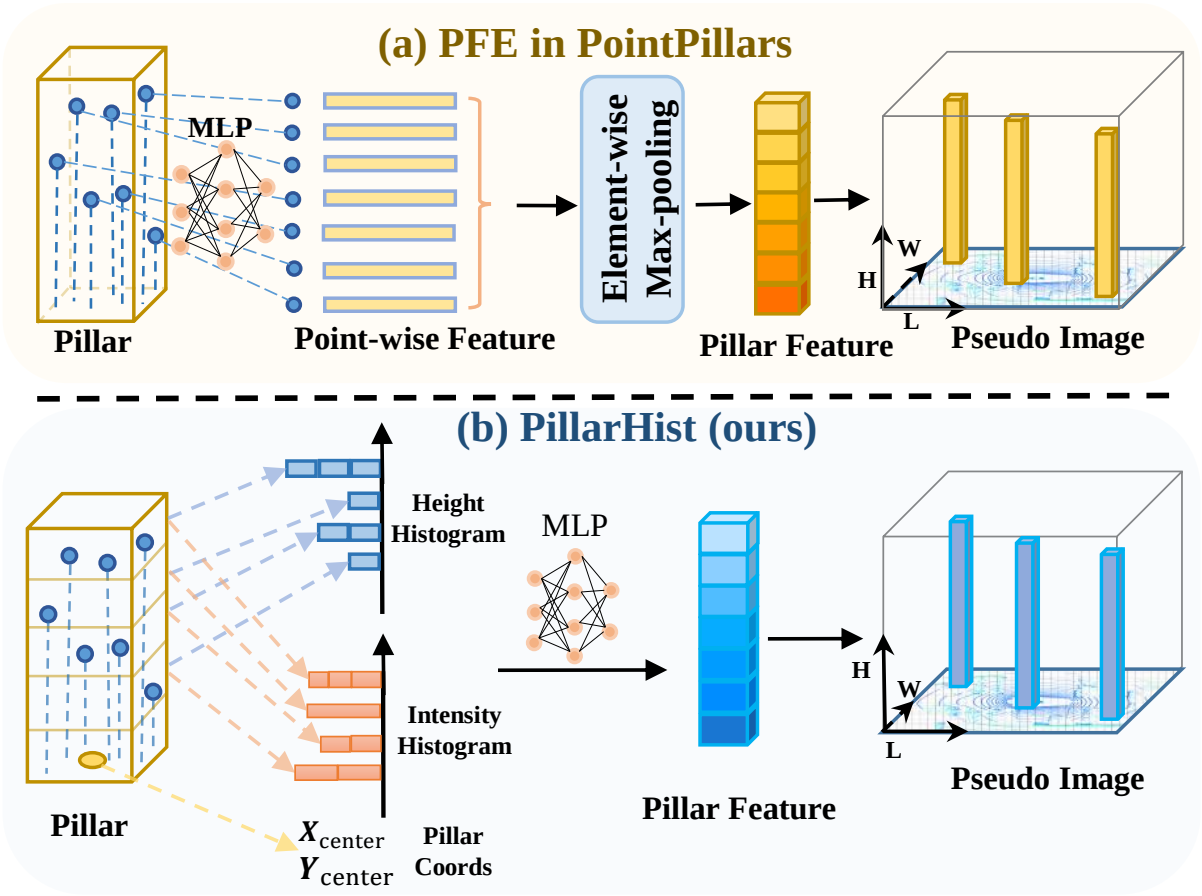

Fig. 3. The overall architecture of our proposed PillarHist. The PFE (a) in PointPillars first extracts point-wise feature, and then the point-wise features are max-pooled along the point dimension to obtain the pillar-wise representation. This process has three key drawbacks: (1) it lacks detailed height-aware information, (2) the MLP operates on point-wise level, incurring computational burden, (3) the max-pooling operation leads to information loss. In contrast, our proposed PillarHist (b) directly encodes the height-aware information based on histogram, and then perform the MLP operation on the pillar level rather than point level. Finally, the max-pooling operation is also eliminated in proposed PillarHist.

signifies a higher density of points near the bottom of the pillar. Conversely, if there is a greater concentration of points in the higher height range bins, it suggests a higher density of points towards the top of the pillar. This approach provides the model with both the semantic and geometric information derived from the height dimension, thereby enhancing its understanding and representation of the point cloud data.

By using the histogram technique, we propose a height-aware pillar feature encoder named PillarHist. The algorithm is summarized: **(1)** We compute the histogram of each pillar, denoted as $H^p \in \mathbb{R}^B$, where B is the number of bins. **(2)** In addition, we incorporates the LiDAR reflection intensity of each point, r_i, to obtain the weighted histogram of intensity, denoted as $H^i \in \mathbb{R}^B$. The weighted histogram represents the mean LiDAR reflection intensity for each bin, providing valuable height-aware information for object detection. **(3)** To provide the global position of each pillar, we utilize the x and y coordinates of the pillar center, x_{center} and y_{center}. Since the coordinates of the pillar are constant, this step does not require any additional computational effort. **(4)** We concatenate the computed histograms and the pillar center coordinates, resulting in $[H^p|H^i|x_{center}|y_{center}] \in \mathbb{R}^{2B+2}$. **(5)** To represent the features of the pillars, we utilize a linear layer f_θ that projects the combined information into a feature vector. $\theta \in \mathbb{R}^{D\times(2B+2)}$ and D is the number of output channels.

Specifically, the pillar center x_{center} and y_{center} provide the relative spatial relationships between different points within the point cloud. This spatial location information of the pillars reflects the relative position of the targets in the scene, which can help the model better understand environmental context. For instance, if there are two pillars with the same point cloud distribution located at [0,10] and [10,0] in space, without the pillar coordinate to indicate the spatial relationship, these two pillars would be indistinguishable. This would pose significant challenges for the detector's object perception capabilities. Therefore, combining pillar center x_{center} and y_{center} with other features such as height and intensity can further enhance the model's perception capability. This is necessary to compensate for the missing spatial position information inherent in the raw point cloud data. By incorporating the pillar center coordinates, the model can better capture the geometric structure and spatial relationships between different parts of the scene. This is a crucial aspect for enabling accurate object detection in point cloud data.

As shown in Fig 3, our PillarHist approach explicitly captures

the histogram of points in different height intervals. This allows us to keep the semantic and geometric information within the pillar. PillarHist operates only during the PFE stage without introducing complex operations or interaction with other modules, allowing for seamless inserted into existing pillar-based methods serves as a plugin module with performance improvements.

The Selection of Bins Number Based on Information Entropy: After the PillarHist encoding, a critical issue arises regarding the selection of the appropriate number of bins B. Using an smaller number of bins can lead to information loss, while excessively large bins for histogram can introduce redundant parameters, posing additional optimization challenges, which might hinder the model's learning capacity in some scenarios. Specifically, similar issues do not exist only in our method. Existing methods generally suffer from such problems, for example, in Voxel-based methods [11], [46]–[48], they need to set the voxel size along the height direction to partition the height. They still require setting different voxel size parameters to adapt to different scenarios and datasets. Different with existing methods, we analyze the impact of the bin number on the information encoding within each pillar from information entropy perspective.

Considering a point cloud data within a height range of H, if we use B bins to encode the height information, the height value of each bin would be $\frac{H}{B}$. The probability distribution of the point cloud count within each bin can be expressed as $p(x) = \frac{n_i}{N_v}$, where n_i is the number of points in the i-th bin, and N_v is the total number of points in current pillar. The information entropy of the point cloud height distribution within a pillar can be formulated as:

$$\begin{aligned} H(V) &= -\sum_{i=1}^{B} p(x)\log p(x) \\ &= -\sum_{i=1}^{B}\left(\frac{n_i}{N_v}\right)\log\left(\frac{n_i}{N_v}\right) \\ &= \log N_v - \left(\frac{1}{N_v}\right)\sum_{i=1}^{B} n_i \log n_i \end{aligned} \tag{4}$$

where $p(x)$ represents the probability density function of the point cloud height distribution, the entropy value $H(V)$ will decrease as the number of bins B increases. This is because the more refined height encoding results in smaller n_i values for each bin, leading to larger log n_i terms, and consequently, a higher entropy value $H(V)$. However, it is important to note that when B increases to a certain degree, the point cloud count n_i within each bin will approach 1, causing the log n_i term to approach 0, and the entropy value $H(V)$ to reach saturation and no longer decrease. This explains the existence of an optimal number of bins. Employing too few bins will be unable to sufficiently represent the height information, leading to information loss, while using too many bins may introduce extra optimization parameters and degrade the model's generalization capability. This is consistent with our ablation study in Table VIII. This more detailed analysis should further elucidate the theoretical foundation of our PillarHist and the importance of selecting the appropriate bin count.

The Efficiency of PillarHist: Here, we further analyze the efficiency of PillarHist. **(1)**. The linear projection in PillarHist operates on the pillar level, not on individual points. In contrast, the previous approach [13], [20], [21], [36] performed the linear projection for each point within a pillar. By employing the linear projection at the pillar level, we significantly decrease the number of floating-point operations (FLOPs) required by the PFE, resulting in improved efficiency (shown in Table VI). **(2)**. PillarHist also avoids various memory-intensive operations, such as copying the original point cloud data, calculating distances $(x^m, y^m, z^m, x^c, y^c, z^c)$, and performing max pooling. This further enhances the efficiency of PillarHist in real-world deployment.

IV. Experiments

A. Dataset

KITTI Dataset. The nuScenes dataset uses a LiDAR with 64 channels. The KITTI has 7481 training samples and 7518 test samples. The training samples are split into a $train$ set with 3,717 samples and a val set with 3,769 samples following the common setting [11]–[13], [56]. The detected boxes are classified into three subsets: "Easy", "Moderate" and "Hard" based on the levels of difficulty. We report Mean Average Precision (mAP).

nuScens Dataset. The nuScenes [24] dataset contains 700 training scenes, 150 val scenes and 150 test scenes. Each frame is generated approximately 30K points by a 32 channels LiDAR sampled with 20Hz. The training, validation and testing set have 28K, 6K and 6K annotated keyframes, respectively, It contains 10 categories in total. Its main ranking metric is the nuScenes detection score (NDS). The Mean Average Precision (mAP) [57] was also used based on distances between the centers of the predictions and ground-truths on the bird-eye view at thresholds 0.5m, 1m, 2m, and 4m.

B. Training Details.

We utilize the Adam optimizer with one-cycle learning rate policy [58]. The initial learning rate is set to 10e-4 during training. The learning rate gradually increases to 0.001 in the first 50% epochs and then gradually decreases to 10e-5 for the remaining training process. We set the weight decay to 0.01 and the momentum to a range of 0.85 to 0.95, For data augmentation, the whole point cloud is flipped randomly along the X axis, randomly is rotated along the Z axis in the range $[-\pi/4, \pi/4]$, and globally is scaled by a random factor sampled from $[0.95, 1.05]$. Regarding the pillar size, network architecture and loss function, we directly follow the setting of the four well-known pillar-based 3D detectors. (*i.e.*, PointPillars [13], CenterPoint-Pillar [20], PillarNet [21], FastPillars [23]). Our experiments are executed on 4 Nvidia Tesla V100 GPUs. We adopt OpenPCDet [59] as the training framework and faithfully reproduced the different baseline methods based on the provided official setting on kitti and nuScenes dataset in the OpenPCDet [59].

C. Quantization Details.

In nuScenes [24] dataset, we uniformlly sample 64 frames point cloud data from the validation set as the calibration set.

TABLE II
PERFORMANCE OF 3D OBJECT DETECTION METHODS ON NUSCENES *test* SET. † MEANS THE METHOD THAT USES DOUBLE-FLIP TESTING. ALL MODELS LISTED TAKE LIDAR DATA AS INPUT WITHOUT IMAGE FUSION OR ANY MODEL ENSEMBLE.

Method	NDS	mAP	Latency	Car	Truck	Bus	Trailer	C.V.	Ped.	Mot	Byc	T.C.	Bar
PointPillars [13]	45.3	30.5	31 ms	68.4	23.0	28.2	23.4	4.1	59.7	27.4	1.1	30.8	38.9
3DSSD [8]	56.4	42.6	-	81.2	47.2	61.4	30.5	12.6	70.2	36.0	8.6	31.1	47.9
CGBS [27]	63.3	52.8	80 ms	81.1	48.5	54.9	42.9	10.5	80.1	51.5	22.3	70.9	65.7
CVCNet [49]	64.2	55.8	122 ms	82.6	49.5	59.4	51.1	16.2	83.0	61.8	38.8	69.7	69.7
CenterPoint [20]	65.5	58.0	96 ms	84.6	51.0	60.2	53.2	17.5	83.4	53.7	28.7	76.7	70.9
HotSpotNet [50]	66.0	59.3	-	83.1	50.9	56.4	53.3	23.0	81.3	63.5	36.6	73.0	71.6
AFDetV2 [51]	68.5	62.4	-	86.3	54.2	62.5	58.9	26.7	85.8	63.8	34.3	80.1	71.0
UVTR-L [52]†	69.7	63.9	132 ms	86.3	52.2	62.8	59.7	33.7	84.5	68.8	41.1	74.7	74.9
VISTA [53]†	69.8	63.0	94 ms	84.4	55.1	63.7	54.2	25.1	82.8	70.0	45.4	78.5	71.4
Focals Conv [54]	70.0	63.8	138 ms	86.7	56.3	67.7	59.5	23.8	87.5	64.5	36.3	81.4	74.1
VoxelNeXt [55]	70.0	64.5	66 ms	84.6	53.0	64.7	55.8	28.7	85.8	73.2	45.7	79.0	74.6
VoxelNeXt [55]†	71.4	66.2	-	85.3	55.7	66.2	57.2	29.8	86.5	75.2	48.8	80.7	76.1
PillarNet-18 [21]†	70.8	65.0	78 ms	87.4	56.7	60.9	61.8	30.4	87.2	67.4	40.3	82.1	76.0
PH-PillarNet-18†	**71.5**	**65.2**	73 ms	87.6	57.0	60.8	62.0	30.6	87.3	68.1	40.3	81.9	76.2
PillarNet-34 [21]†	71.4	66.0	96 ms	87.6	57.5	63.6	63.1	27.9	87.3	70.1	42.3	83.3	77.2
PH-PillarNet-34†	**72.0**	**66.3**	92 ms	87.5	57.6	64.0	63.3	28.4	87.1	70.5	43.0	83.6	77.8

The calibration set proportions is **1.06%** (64/6019). We set the first and the last layer of the network to keep full precision. We do not consider using Int8 quantization in MLP within PillarHist/PFE, since the input is discrete 3D coordinates. We execute all experiments on a single Nvidia Tesla V100 GPU. Please refer to appendix for more quantization details.

D. Overall Results

To evaluate the effectiveness and generalization ability of our proposed PillarHist, we use three popular pillar-based 3D detectors, PointPillars [13], Center-Point-Pillar [20], and PillarNet [21], as our baseline models.

Evaluation on nuScenes test set. The quantitative results on nuScenes *test* set are shown in Table II. It can be seen that by integrating our proposed PillarHist into the current state-of-the-art pillar-based detector PillarNet [21] (*e.g.*, PH-PillarHist), the proposed PH-PillarHist outperforms other approaches and achieves state-of-the-art performance on nuScenes test set, increasing 0.7 NDS and 0.2 mAP on PillarNet-18 and 0.6 NDS and 0.3 mAP on PillarNet-34, respectively. Meanwhile, PH-PillarHist brings 5ms and 4ms reduction on inference latency (78ms $\rightarrow$ 73ms on PillarNet-18 and 96ms $\rightarrow$ 92ms on PillarNet-34). Notably, in this paper, we focus on the pillar feature encoding module, rather than aiming to design a state-of-the-art pillar-based detector. The proposed PillarHist is a plugin module to conveniently insert into existing mainstream pillar-based methods, seamlessly bringing performance gains and latency reduction. This presents the effectiveness and efficiency of PillarHist in not only boosting the detection accuracy, but also improving the computational efficiency, making it practical for real-world application.

Generalization of PillarHist on nuScenes val set. Here, we evaluate our PillarHist's generalization on different pillar-based baselins in nuScenes val set. We selected three representative pillar-based detectors: PointPillars [13], CP-Pillar [20], and PillarNet [21]. In detail, we replace the raw PFE module in each baseline model with our proposed PillarHist, resulting in PH-PointPillars, PH-CP-Pillar, and PH-PillarNet, respectively. As shown in Table III, the results demonstrate the generalizability of proposed PillarHist, as we observe performance improvements of 1.7 NDS, 1.4 NDS, and 1.6 NDS on the three differnet baselin models, respectively. These results highlight the effectiveness and broad applicability of our PillarHist module in enhancing the representation power of pillar-based 3D object detectors, leading to consistent performance gains across different baseline architectures.

Notably, On the nuScenes dataset, the nuScenes detection score (NDS) is the primary evaluation metric. As shown in Table III, our proposed method achieves consistent performance gains on the NDS across different pillar-based 3D object detectors. The key contribution that leads to the NDS improvement is the significant reduction in the Mean Average Orientation Error (mAOE) and Mean Average Velocity Error (mAVE), indicating that our method is effective in mitigating the orientation and velocity estimation errors of the detected objects. The improvements can be attributed to the enhanced ability of our PillarHist encoder to capture the spatial and structural information of the point cloud within each pillar. The performance gains on the NDS metric, which reflects the overall detection quality, demonstrate the effectiveness of our proposed PillarHist in improving the robustness and accuracy of pillar-based 3D object detectors on the nuScenes benchmark.

The Quantization-friendly Effectiveness of PillarHist. Here, we conduct quantization experiments on different pillar-based baselines to evaluate the quantization-friendly characteristics. Specifically, we converted the weights and activations of the models from floating-point 32-bit to integer 8-bit and applied a simple post-training quantization setting to compress. As shown in Table IV, we find that the PointPillars, CP-Pillar, and PillarNet models suffered significant performance degradation after weight and activation quantization, with drops of 7.3 NDS and 7.6 mAP for PointPillars, 7.8 NDS and 8.7

TABLE III
GENERALIZATION AND QUANTIZATION PERFORMANCE COMPARISON ON NUSCENE *val* SET.

Models	NDS↑	mAP↑	mATE↓	mASE↓	mAOE↓	mAVE↓	mAAE↓
PointPillars [13]	52.1	37.4	0.374	0.266	0.407	0.410	0.202
PH-PointPillars	**53.8** (+1.7)	**38.8** (+1.4)	0.366	0.262	0.387	0.337	0.204
CP-Pillar [20]	56.4	44.9	0.336	0.266	0.532	0.289	0.189
PH-CP-Pillar	**57.8** (+1.4)	**45.8** (+0.9)	0.330	0.264	0.514	0.215	0.188
PillarNet [21]	61.4	52.6	0.296	0.262	0.502	0.250	0.186
PH-PillarNet	**63.0** (+1.6)	**52.7** (+0.1)	0.296	0.256	0.376	0.217	0.182

TABLE IV
GENERALIZATION AND QUANTIZATION PERFORMANCE COMPARISON ON NUSCENE *val* SET.

Models	Bits (W/A)	NDS	mAP
PointPillars [13]	32/32	52.1	37.4
	8/8	44.8 (**-7.3**)	29.8 (**-7.6**)
PH-PointPillars	32/32	53.8	38.8
	8/8	**52.2** (**-1.6**)	**37.0** (**-1.8**)
CP-Pillar [20]	32/32	56.4	44.9
	8/8	48.6 (**-7.8**)	36.2 (**-8.7**)
PH-CP-Pillar	32/32	57.8	45.8
	8/8	**56.3** (**-1.5**)	**44.3** (**-1.5**)
PillarNet [21]	32/32	61.4	52.6
	8/8	54.6 (**-6.8**)	43.1 (**-9.5**)
PH-PillarNet	32/32	63.0	52.7
	8/8	**61.6** (**-1.4**)	**51.4** (**-1.3**)

mAP for CP-Pillar, and 6.8 NDS and 9.5 mAP for PillarNet. In contrast, the PH-PointPillars, PH-CP-Pillar, and PH-PillarNet models that integrate PillarHist only perform performance drops of 1.6 NDS, 1.5 NDS, and 1.4 NDS, respectively. Notably, the quantized models with PillarHist integration achieved comparable performance to original floating-point counterparts without PillarHist (52.2 *v.s.* 52.1 NDS on PointPillars, 56.3 *v.s.* 56.4 NDS on CenterPoint-Pillars and 61.6 *v.s.* 61.4 NDS on PillarNet). Specifically, PillarHist could effectively eliminate the severe performance degradation after quantization caused by their PFE design, bringing quantization performance gain seamlessly. These results demonstrate the quantization-friendly nature of PillarHist, which maintains the model's representation power and performance even under quantization compression. This property is particularly valuable and practicable for deploying high-performance 3D object detectors on resource-constrained edge devices, where accuracy and latency are critical factors.

Generalization of PillarHist on KITTI val set. As shown in Table V, when compared to pointpillars [13], CenterPoint-Pillar [20], and PillarNet [21] methods, our method achieves mAP improvements of 1.43, 0.84, and 0.70 for the vehicle class, respectively. For the pedestrian category, PillarHist achieves even larger performance gains of 1.66, 2.02, and 1.62 points on mAP, respectively. These improvements indicate that our histogram-based point feature encoder can generate more informative features to enhance object detection performance.

TABLE V
COMPARISON WITH THE PILLAR-BASED METHODS ON THE KITTI *val* SET.

Methods	Car $3D_{R40}$				Ped $3D_{R40}$			
	mAP	Easy	**Mod.**	Hard	mAP	Easy	**Mod.**	Hard
PointPillars [13]	79.98	87.08	77.90	74.97	49.41	54.71	49.01	44.52
PH-PointPillars	81.41	88.80	79.13	76.30	51.07	57.45	50.42	45.36
⇑	**1.43**	**1.72**	**1.23**	**1.33**	**1.66**	**2.74**	**1.41**	**0.84**
CP-Pillar [20]	77.01	84.70	74.46	71.89	42.91	45.74	42.93	39.76
PH-CP-Pillar	77.85	85.62	75.17	72.77	44.93	49.10	44.99	40.72
⇑	**0.84**	**0.92**	**0.71**	**0.88**	**2.02**	**3.36**	**2.06**	**0.96**
PillarNet [21]	80.90	87.21	79.05	76.44	44.51	47.83	44.80	41.01
PH-PillarNet	81.60	88.71	79.05	77.03	46.10	49.75	45.96	42.61
⇑	**0.70**	**1.50**	0.00	**0.59**	**1.62**	**1.92**	**1.16**	**1.60**

E. Ablation Study

Comparison of Different PFE modules. We compare the computation efficiency and performance of existing PFE modules. Specifically, we evaluate the following PFE modules: PFE module in PointPillars [13], DynPFE module in CenterPoint-Pillar [20], TA module in TANet [36], PAA module in PiFeNet [37], DynPFE module in PillarNet [21] (denoted as DynPFE*), and MAPE module in FastPillars [23]. To ensure a fair comparison, we select PointPillars as the baseline method and conduct experiments by replacing the PFE module in PointPillars with other PFE module (DynPFE, TA, PAA, DynpFE*, MAPE and our PillarHist). This setting eliminates the performance difference caused by different backbone and regression heads. As shown in Table VI, our PillarHist achieves the highest 3D AP compared to other PFE methods while maintaining superior computational efficiency. In comparison to the PFE in PointPillars [13], PillarHist demonstrates significant performance improvements of 1.44 and 1.66 for vehicle and pedestrian, respectively, while utilizing only approximately 40% of the computational cost in terms of GFLOPs. It is worth noting that although DynPFE$*$ used in PillarNet [21] has lower GFLOPs, it suffers from poor detection performance.

Specifically, the TA module [36] in TANet and PAA module in PiFeNet [37] focus on the pillar feature encoding, while all operating on point-wise level and inevitably using pooling operation. This point-wise processing bring a large computational burden and also limits the pillar representations. In contrast, our proposed PillarHist method performs linear projection at the pillar-wise level rather than point-wise level. This design choice can efficiently reduce the computational cost while maintaining the necessary structural information within each pillar without pooling operations. Therefore, PillarHist is able to capture the salient geometric properties of the point cloud in a more computationally efficient manner compared to point-wise processing.

TABLE VI
PERFORMANCE OF DIFFERENT PFE MODULES ON THE KITTI *val* SET IN AP_{3D} (R40).

PFE module	Car $3D_{R40}$ mAP	Easy	**Mod.**	Hard	Ped $3D_{R40}$ mAP	Easy	**Mod.**	Hard	PFE GFLOPs
PFE [13]	79.98	87.08	77.90	74.97	49.41	54.71	49.01	44.52	0.152
DynPFE [20]	80.46	87.86	78.16	75.38	47.77	52.28	47.53	43.52	0.112
TA [36]	80.71	87.33	79.11	75.69	49.45	54.00	49.31	45.05	7.061
PAA [37]	81.04	88.62	79.24	75.27	48.56	54.26	47.93	43.49	3.391
DynPFE* [21]	79.96	87.63	77.70	74.55	49.36	54.27	49.01	44.81	0.013
MAPE [23]	81.19	89.39	78.57	75.63	48.18	52.68	48.02	43.83	0.165
PillarHist	**81.42**	88.80	**79.13**	76.30	**51.07**	57.45	**50.42**	45.36	0.065

TABLE VII
PERFORMANCE OF SPECIFIC PFE MODULES ON THE KITTI *test* SET IN AP_{3D} (R40) FOR *Pedestrian*.

Method	**3D Detection** **Easy**	**Mod.**	**Hard**	**mAP**	**FPS**
PointPillars [13]	51.45	41.92	38.89	44.09	63
TANet [36]	53.72	44.34	40.49	46.18	29
PiFeNet [37]	56.39	46.71	42.71	**48.60**	26
PH-PointPillars (Ours)	55.79	45.85	42.15	47.93	**69**

TABLE VIII
ABLATION STUDY ON THE NUMBER OF BINS s ON THE KITTI *val* SET IN AP_{3D} (R40).

bins	Car $3D_{R40}$ mAP	Easy	**Mod.**	Hard	Ped $3D_{R40}$ mAP	Easy	**Mod.**	Hard
s=16	80.27	87.57	78.15	75.10	45.79	50.35	45.62	41.41
s=32	80.49	87.98	78.28	75.22	49.79	55.35	49.48	44.56
s=48	81.24	89.31	78.69	75.74	50.08	55.42	49.91	44.93
s=64	**81.41**	88.80	**79.13**	76.30	**51.07**	57.45	**50.42**	45.36
s=80	80.49	87.53	78.44	75.50	49.96	55.82	49.68	44.38

Comparison with Specific PFE Methods on KITTI test set. Existing methods that focus solely on pillar encoding include TANet [36] and PiFeNet [37], where PiFeNet is tailored specifically for pedestrian detection. To enable a fair comparison, we report the pedestrian category performance on the KITTI test set. We follow the experiment setting of PiFeNet, where the training set is further split into training and validating set with a ratio of 85:15. We select PointPillars as our baseline and only replaced its pillar feature encoding module with our PillarHist to construct **PH-PointPillars** for comparison. As shown in Table VII, our method achieves a 3.84 AP improvement over the baseline (PointPillars) and is 1.75 AP higher than TANet. Compared to PiFeNet, PH-PointPillars achieve comparable performance at 2.7 times the inference speed of PiFeNet, which confirms the effectiveness and efficiency of our PillarHist design. For PiFeNet, although our method's performance was slightly lower (0.73 AP lower), we believe this is because we didn't selecting a better backbone and bounding box regression structure design due to we focuse on pillar feature encoding design. In contrast, the TANet and PiFeNet in Table VII, in addition to their TA module and PAA module design, they also include Coarse-to-Fine Regression (CFR) and Mini-BiFP design for feature encoding and bounding box regression, those extra designs have been shown to be effective than the PointPillar backbone in their paper, respectively.

The Number of Bins Along Height Dimension. Here, we conduct an ablation study on the number of bins s in the height dimension. We take PointPillars as our baseline. Notably, PointPillars limits the maximum number of points as 32 in each pillar. We vary the number of bins from 16 to 80, and the results are presented in Table VIII. As the number of bins increased, the performance of the model improved steadily. However, the performance does not exhibit a monotonic improvement trend and exhibit a degradation when the number of bins was increased to 80. Although larger number of bins can better encode discriminative features in the height dimension, the performance saturates when the number of bins becomes excessively large. This results is consistent with our analysis in Sec III-C: the information entropy will decrease as the number of bins B increases, but will eventually saturate and no longer decrease. Conversely, introducing too many parameters may pose additional optimization challenges, thereby hindering the model's learning capacity. Based on these experimental results, we selected a value of 64 for the number of bins.

The Effects of Different Feature in PillarHist. Here, we conduct ablation study to analyze the impact of different input information in PillarHist. As depicted in the first and second rows in Table IX, when we incorporate the intensity information of points into pillar feature, it leads to performance improvements for both the vehicle and pedestrian categories. Particularly for the pedestrian, there are significant performance improvements of approximately 1.7, 1.6, and 1.6 points in average precision (AP) for the easy, moderate, and hard levels, respectively. This notable improvement indicates that for small objects like pedestrians, the intensity values are crucial in distinguishing them from the background and enhancing their distinctive features. As shown in the second and third rows of the Table IX, by adding the pillar coordinates information, there is a performance improvement of 0.6 and 1.45 points in AP for the vehicle and pedestrian categories. We believe this improvement is because explicitly incorporating the global coordinate of the pillars during PFE helps the model better identify the object positions with the enhanced encoding information that includes height awareness. Notably, after adding the pillar coordinates, there is an improvement of 2.03 points in easy AP for pedestrians. This can be ascribed to the fact that the pillars encode not only varying height distribution information but also including the difference between empty

TABLE IX
ABLATION RESULTS OF DIFFERENT INPUT FOR PILLARHIST ON THE KITTI *val* SET FOR CAR AND PEDESTRIAN.

height	intensity	pillar coords	Car $3D_{R40}$ mAP	Easy	Mod.	Hard	Ped $3D_{R40}$ mAP	Easy	Mod.	Hard
✔			80.18	87.47	78.18	75.22	48.06	53.75	47.51	42.92
✔	✔		80.81	88.29	78.62	75.53	49.62	55.42	49.10	44.36
✔	✔	✔	**81.41**	88.80	**79.13**	76.30	**51.07**	57.45	**50.42**	45.36

and non-empty pillars.

TABLE X
APPLY PILLARHIST TO CETERPOINT-PILLARS ON WAYMO *val* SET TRAINED WITH 20% TRAINING DATA.

Methods	Mean (L2) mAPH	Vehicle (L2) mAP	Vehicle (L2) mAPH	Ped. (L2) mAP	Ped. (L2) mAPH	Cyc. (L2) mAP	Cyc. (L2) mAPH
CP-Pillar	55.9	62.5	62.0	61.8	51.5	56.1	54.3
PH-CP-Pillar	57.3	63.2	62.8	63.8	54.0	57.0	55.3
⇑	**+1.4**	**+0.7**	**+0.8**	**+2.0**	**+2.5**	**+0.9**	**+1.0**

Generalization of PillarHist on Waymo val set. Here, we also conduct the ablation experiments on Waymo dataset to evaluate the effectiveness of PillarHist. We select CenterPoint-Pillars as our baseline and only replaced its pillar feature encoding module with our PillarHist for comparison, as show in table our method can bring 1.2 mAP L2 and 1.5 mAPH L2 performance improvements. Notably, it can achieve 2.0 mAP L2 and 2.5 mAPH L2 performance gains in the pedestrian category. This result demonstrates the effectiveness of our method.

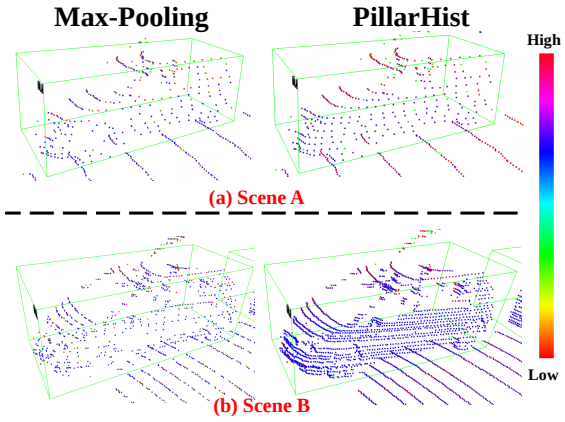

Fig. 4. Visualization of the learned attention scores in PillarHist on different scenes. The color of points represents their scores. The point will be paid more attention if it has a higher score. Best viewed in color.

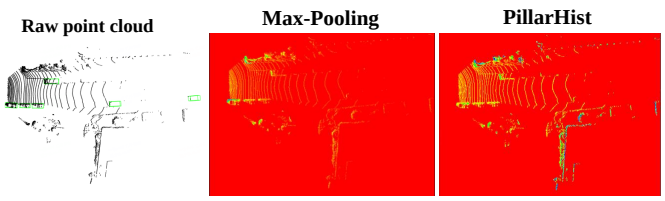

Fig. 5. Visualization of the learned BEV feature in PointPillars and PH-PointPillars.

Feature Map Visualization of PillarHist. Here, as shown in Figure 4, we apply our PillarHist method to PointPillars and we compare the features of our PillarHist against the features from the max-pooling operation (PFE module in PointPillars [13]). We find that the max pooling operation tends to focus more on the points at higher positions within the same pillar, resulting in a biased feature representation. In contrast, our PillarHist can focus more evenly on each point within the pillar, encoding the height information into an unbiased histogram distribution, thereby obtaining richer geometric-semantic feature representation. Besides, as shown in Figure 5, we also visualize the BEV features maps. Our method can obtain a more informative BEV feature representation compared to the max-pooling (PFE in PointPillars) operation. This also demonstrates the underlying reason for the better performance of our method.

TABLE XI
THE EFFECTS OF PILLARHIST ON SECOND [12] ON THE KITTI *val* SET.

Methods	Car $3D_{R40}$ mAP	Easy	**Mod.**	Hard	Ped $3D_{R40}$ mAP	Easy	**Mod.**	Hard
SECOND [12]	83.59	90.55	81.61	78.60	51.08	55.94	51.14	46.17
PH-SECOND	83.96	91.04	81.95	78.90	51.41	56.38	51.82	46.03
⇑	**+0.37**	**+0.49**	**+0.34**	**+0.30**	**+0.33**	**+0.44**	**+0.68**	-

The Effects of PillarHist on Voxel-based Detectors. As shown in Table XI, we integrate PillarHist into SECOND [12], a representative voxel-based 3D object detector. The results demonstrate that the proposed PillarHist can still lead to performance improvements for voxel-based methods, albeit with slight margin compared to the gains observed for pillar-based detectors. We conjecture that this can be attributed to the inherent design of voxel-based methods. Specifically, voxel-based approaches explicitly encode height information by discretizing the input point cloud into voxel features along the height dimension, which are then processed using 3D CNN. Therefore, further encoding finer-grained height statistics within each voxel may not yield substantial performance benefits due to the sparsity of point clouds, as the height-aware features are already captured by the underlying voxel representation.

V. CONCLUSION

In this paper, we addressed the issue of information loss and large numerical distribution difference in existing pillar-based 3D object detectors during the PFE stage. We identify the height dimension as a crucial factor for enhancing 3D detection performance and proposed a height-aware pillar feature encoder called PillarHist. By leveraging a histogram technique, PillarHist preserved the information along the height dimension while effectively mitigating the information loss introduced by max-pooling operations. Importantly, PillarHist operated exclusively within the PFE stage, allowing seamless insert

into existing pillar-based methods serves as a plugin module. Meanwhile, PillarHist also constrains the arithmetic distribution of PFE input to a stable range, making it quantization-friendly. Extensive experiments demonstrated the effectiveness of PillarHist in terms of both efficiency and performance. Our proposed method achieved an average improvement of approximately 1.5% NDS across various baselines, showcasing its ability to enhance 3D object detection accuracy. The code for PillarHist will be released.

REFERENCES

[1] Z. Tian, X. Chu, X. Wang, X. Wei, and C. Shen, "Fully convolutional one-stage 3d object detection on lidar range images," *NeurIPS*, 2022.

[2] S. Zhou, L. Li, X. Zhang, B. Zhang, S. Bai, M. Sun, Z. Zhao, X. Lu, and X. Chu, "Lidar-ptq: Post-training quantization for point cloud 3d object detection," *International Conference on Learning Representations (ICLR)*, 2024.

[3] J. Shan, S. Zhou, Z. Fang, and Y. Cui, "Ptt: Point-track-transformer module for 3d single object tracking in point clouds," in *2021 IEEE/RSJ International Conference on Intelligent Robots and Systems (IROS)*. IEEE, 2021, pp. 1310–1316.

[4] Z. Fang, S. Zhou, Y. Cui, and S. Scherer, "3d-siamrpn: An end-to-end learning method for real-time 3d single object tracking using raw point cloud," *IEEE Sensors Journal*, vol. 21, no. 4, pp. 4995–5011, 2020.

[5] S. Jiayao, S. Zhou, Y. Cui, and Z. Fang, "Real-time 3d single object tracking with transformer," *IEEE Transactions on Multimedia*, 2022.

[6] W. Shi and R. Rajkumar, "Point-gnn: Graph neural network for 3D object detection in a point cloud," in *CVPR*, 2020, pp. 1711–1719.

[7] C. R. Qi, O. Litany, K. He, and L. J. Guibas, "Deep hough voting for 3D object detection in point clouds," in *ICCV*, 2019, pp. 9277–9286.

[8] Z. Yang, Y. Sun, S. Liu, and J. Jia, "3dssd: Point-based 3D single stage object detector," in *CVPR*, 2020, pp. 11 040–11 048.

[9] L. Fan, F. Wang, N. Wang, and Z.-X. ZHANG, "Fully sparse 3d object detection," *Advances in Neural Information Processing Systems*, vol. 35, pp. 351–363, 2022.

[10] S. Shi, Z. Wang, J. Shi, X. Wang, and H. Li, "From points to parts: 3d object detection from point cloud with part-aware and part-aggregation network," *IEEE T-PAMI*, 2020.

[11] Y. Zhou and O. Tuzel, "Voxelnet: End-to-end learning for point cloud based 3D object detection," in *CVPR*, 2018, pp. 4490–4499.

[12] Y. Yan, Y. Mao, and B. Li, "Second: Sparsely embedded convolutional detection," *Sensors*, vol. 18, no. 10, p. 3337, 2018.

[13] A. H. Lang, S. Vora, H. Caesar, L. Zhou, J. Yang, and O. Beijbom, "Pointpillars: Fast encoders for object detection from point clouds," in *CVPR*, 2019, pp. 12 697–12 705.

[14] J. Deng, S. Shi, P. Li, W. Zhou, Y. Zhang, and H. Li, "Voxel r-cnn: Towards high performance voxel-based 3D object detection," in *AAAI*, 2021.

[15] J. Mao, Y. Xue, M. Niu, H. Bai, J. Feng, X. Liang, H. Xu, and C. Xu, "Voxel transformer for 3d object detection," in *ICCV*, 2021, pp. 3164–3173.

[16] H. Kuang, B. Wang, J. An, M. Zhang, and Z. Zhang, "Voxel-fpn: Multi-scale voxel feature aggregation for 3d object detection from lidar point clouds," *Sensors*, vol. 20, no. 3, p. 704, 2020.

[17] C. R. Qi, H. Su, K. Mo, and L. J. Guibas, "Pointnet: Deep learning on point sets for 3D classification and segmentation," in *CVPR*, 2017, pp. 652–660.

[18] T. Yin, X. Zhou, and P. Krahenbuhl, "Centerpoint++ submission to the waymo real-time 3d detection challenge," 2021, accessed: 2021-12-05.

[19] C. R. Qi, L. Yi, H. Su, and L. J. Guibas, "Pointnet++: Deep hierarchical feature learning on point sets in a metric space," in *NeurIPS*, 2017, pp. 5099–5108.

[20] T. Yin, X. Zhou, and P. Krahenbuhl, "Center-based 3d object detection and tracking," in *CVPR*, 2021, pp. 11 784–11 793.

[21] G. Shi, R. Li, and C. Ma, "Pillarnet: Real-time and high-performance pillar-based 3d object detection," in *ECCV*, 2022.

[22] J. Li, C. Luo, and X. Yang, "Pillarnext: Rethinking network designs for 3d object detection in lidar point clouds," in *IEEE/CVF Conference on Computer Vision and Pattern Recognition (CVPR)*, 2023.

[23] S. Zhou, Z. Tian, X. Chu, X. Zhang, B. Zhang, X. Lu, C. Feng, Z. Jie, P. Y. Chiang, and L. Ma, "Fastpillars: A deployment-friendly pillar-based 3d detector," *arXiv preprint arXiv:2302.02367*, 2023.

[24] H. Caesar, V. Bankiti, A. Lang, S. Vora, V. E. Liong, Q. Xu, A. Krishnan, Y. Pan, G. Baldan, and O. Beijbom, "Nuscenes: A multimodal dataset for autonomous driving," in *CVPR*, 2020, pp. 11 621–11 631.

[25] Y. Guo, H. Wang, Q. Hu, H. Liu, L. Liu, and M. Bennamoun, "Deep learning for 3d point clouds: A survey," *IEEE Transactions on Pattern Analysis and Machine Intelligence*, vol. 43, no. 12, pp. 4338–4364, 2021.

[26] J. Mao, S. Shi, X. Wang, and H. Li, "3d object detection for autonomous driving: A comprehensive survey," *International Journal of Computer Vision*, pp. 1–55, 2023.

[27] B. Zhu, Z. Jiang, X. Zhou, Z. Li, and G. Yu, "Class-balanced grouping and sampling for point cloud 3d object detection," *arXiv:1908.09492*, 2019.

[28] Y. Wang and J. M. Solomon, "Object dgcnn: 3d object detection using dynamic graphs," *NeurIPS*, 2021.

[29] W. Zheng, W. Tang, S. Chen, L. Jiang, and C.-W. Fu, "Cia-ssd: Confident iou-aware single-stage object detector from point cloud," in *AAAI*, 2021.

[30] Y. Tian, L. Huang, H. Yu, X. Wu, X. Li, K. Wang, Z. Wang, and F.-Y. Wang, "Context-aware dynamic feature extraction for 3d object detection in point clouds," *IEEE Transactions on Intelligent Transportation Systems*, vol. 23, no. 8, pp. 10 773–10 785, 2021.

[31] M. Ye, S. Xu, and T. Cao, "Hvnet: Hybrid voxel network for lidar based 3d object detection," in *Proceedings of the IEEE/CVF conference on computer vision and pattern recognition*, 2020, pp. 1631–1640.

[32] T. Wang, X. Zhu, and D. Lin, "Reconfigurable voxels: A new representation for lidar-based point clouds," *arXiv preprint arXiv:2004.02724*, 2020.

[33] Y. Zhou, P. Sun, Y. Zhang, D. Anguelov, J. Gao, T. Ouyang, J. Guo, J. Ngiam, and V. Vasudevan, "End-to-end multi-view fusion for 3d object detection in lidar point clouds," in *Conference on Robot Learning*. PMLR, 2020, pp. 923–932.

[34] C. Wang and Z. Liu, "Cafi-pillars: Infusing geometry priors for pillar-based 3d detectors through centroid-aware feature interaction," *IEEE Transactions on Intelligent Vehicles*, pp. 1–10, 2023.

[35] J. Fu, G. Ren, Y. Chen, and S. Liu, "Improved pillar with fine-grained feature for 3d object detection," *arXiv preprint arXiv:2110.06049*, 2021.

[36] Z. Liu, X. Zhao, T. Huang, R. Hu, Y. Zhou, and X. Bai, "Tanet: Robust 3d object detection from point clouds with triple attention," in *Proceedings of the AAAI Conference on Artificial Intelligence*, vol. 34, no. 07, 2020, pp. 11 677–11 684.

[37] D. T. Le, H. Shi, H. Rezatofighi, and J. Cai, "Accurate and real-time 3d pedestrian detection using an efficient attentive pillar network," *IEEE Robotics and Automation Letters*, vol. 8, no. 2, pp. 1159–1166, 2022.

[38] Y. Zhang, Z. Dong, H. Yang, M. Lu, C.-C. Tseng, Y. Guo, K. Keutzer, L. Du, and S. Zhang, "Qd-bev: Quantization-aware view-guided distillation for multi-view 3d object detection," 2023.

[39] Z. Li, W. Wang, H. Li, E. Xie, C. Sima, T. Lu, Y. Qiao, and J. Dai, "Bevformer: Learning bird's-eye-view representation from multi-camera images via spatiotemporal transformers," in *Computer Vision–ECCV 2022: 17th European Conference, Tel Aviv, Israel, October 23–27, 2022, Proceedings, Part IX*. Springer, 2022, pp. 1–18.

[40] L. Stäcker, J. Fei, P. Heidenreich, F. Bonarens, J. Rambach, D. Stricker, and C. Stiller, "Deployment of deep neural networks for object detection on edge ai devices with runtime optimization," in *Proceedings of the IEEE/CVF International Conference on Computer Vision Workshop*, 2021, pp. 1015–1022.

[41] H. Qin, Z. Cai, M. Zhang, Y. Ding, H. Zhao, S. Yi, X. Liu, and H. Su, "Bipointnet: Binary neural network for point clouds," in *ICLR*, 2021.

[42] M. Nagel, R. A. Amjad, M. Van Baalen, C. Louizos, and T. Blankevoort, "Up or down? adaptive rounding for post-training quantization," in *International Conference on Machine Learning*. PMLR, 2020, pp. 7197–7206.

[43] Y. Li, R. Gong, X. Tan, Y. Yang, P. Hu, Q. Zhang, F. Yu, W. Wang, and S. Gu, "Brecq: Pushing the limit of post-training quantization by block reconstruction," *arXiv preprint arXiv:2102.05426*, 2021.

[44] X. Wei, R. Gong, Y. Li, X. Liu, and F. Yu, "Qdrop: Randomly dropping quantization for extremely low-bit post-training quantization," *arXiv preprint arXiv:2203.05740*, 2022.

[45] J. Liu, L. Niu, Z. Yuan, D. Yang, X. Wang, and W. Liu, "Pd-quant: Post-training quantization based on prediction difference metric," in *Proceedings of the IEEE/CVF Conference on Computer Vision and Pattern Recognition*, 2023, pp. 24 427–24 437.

[46] H. Yi, S. Shi, M. Ding, J. Sun, K. Xu, H. Zhou, Z. Wang, S. Li, and G. Wang, "Segvoxelnet: Exploring semantic context and depth-aware features for 3D vehicle detection from point cloud," in *ICRA*, 2020, pp. 2274–2280.

[47] Z. Liu, H. Tang, Y. Lin, and S. Han, "Point-voxel cnn for efficient 3d deep learning," *arXiv preprint arXiv:1907.03739*, 2019.

[48] J. Deng, S. Shi, P. Li, W. Zhou, Y. Zhang, and H. Li, "Voxel r-cnn: Towards high performance voxel-based 3d object detection," in *AAAI*, 2021.

[49] Q. Chen, L. Sun, E. Cheung, K. Jia, and A. Yuille, "Every view counts: Cross-view consistency in 3d object detection with hybrid-cylindrical-spherical voxelization," *NeurIPS*, 2020.

[50] Q. Chen, L. Sun, Z. Wang, K. Jia, and A. Yuille, "Object as hotspots: An anchor-free 3d object detection approach via firing of hotspots," in *European conference on computer vision*. Springer, 2020, pp. 68–84.

[51] Y. Hu, Z. Ding, R. Ge, W. Shao, L. Huang, K. Li, and Q. Liu, "Afdetv2: Rethinking the necessity of the second stage for object detection from point clouds," in *Proceedings of the AAAI Conference on Artificial Intelligence*, vol. 36, no. 1, 2022, pp. 969–979.

[52] Y. Li, Y. Chen, X. Qi, Z. Li, J. Sun, and J. Jia, "Unifying voxel-based representation with transformer for 3d object detection," in *Advances in Neural Information Processing Systems*, 2022.

[53] S. Deng, Z. Liang, L. Sun, and K. Jia, "Vista: Boosting 3d object detection via dual cross-view spatial attention," in *Proceedings of the IEEE/CVF Conference on Computer Vision and Pattern Recognition*, 2022, pp. 8448–8457.

[54] Y. Chen, Y. Li, X. Zhang, J. Sun, and J. Jia, "Focal sparse convolutional networks for 3d object detection," in *Proceedings of the IEEE Conference on Computer Vision and Pattern Recognition*, 2022.

[55] Y. Chen, J. Liu, X. Zhang, X. Qi, and J. Jia, "Voxelnext: Fully sparse voxelnet for 3d object detection and tracking," in *Proceedings of the IEEE/CVF Conference on Computer Vision and Pattern Recognition*, 2023.

[56] S. Shi, X. Wang, and H. Li, "Pointrcnn: 3D object proposal generation and detection from point cloud," in *CVPR*, 2019, pp. 770–779.

[57] M. Everingham, L. Van Gool, C. K. Williams, J. Winn, and A. Zisserman, "The pascal visual object classes (voc) challenge," *IJCV*, 2010.

[58] L. N. Smith and N. Topin, "Super-convergence: Very fast training of neural networks using large learning rates," in *Artificial intelligence and machine learning for multi-domain operations applications*, vol. 11006. SPIE, 2019, pp. 369–386.

[59] O. D. Team, "OpenPCDet: An open-source toolbox for 3D object detection from point clouds," https://github.com/open-mmlab/OpenPCDet, 2020.